Research Square

Preprints are preliminary reports that have not undergone peer review.
They should not be considered conclusive, used to inform clinical practice,
or referenced by the media as validated information.

The IGF2BP2/HMGA2/FOSL1 Axis Controls Cell Plasticity and Therapy Resistance in Neuroblastoma

Zhixiang Wu

wuzhixiang@xinhuamed.com.cn

Xinhua Hospital Affiliated to Shanghai Jiao Tong University School of Medicine
https://orcid.org/0000-0002-3947-2035

Tian He

Xinhua Hospital, School of Medicine, Shanghai Jiaotong University

Jia Shi

Xinhua Hospital, School of Medicine, Shanghai Jiaotong University

Qichen Liu

Xinhua Hospital, School of Medicine, Shanghai Jiaotong University

Kai Chen

Department of Pediatric Surgery, Xinhua Hospital, School of Medicine, Shanghai Jiaotong University
https://orcid.org/0000-0002-8845-1820

Qianqian Chen

Xinhua Hospital, School of Medicine, Shanghai Jiaotong University

Yujie Tang

Shanghai Jiao Tong University School of Medicine https://orcid.org/0000-0001-7647-5780

Cheng Cheng

Shanghai Jiao Tong University School of Medicine Affiliated Xinhua Hospital

Article

Keywords: Neuroblastoma, Mesenchymal phenotype, Tumor cell plasticity, HMGA2, RNA m⁶A modification

Posted Date: July 29th, 2026

DOI: https://doi.org/10.21203/rs.3.rs-10306203/v1

License: This work is licensed under a Creative Commons Attribution 4.0 International License.
Read Full License

Additional Declarations: (Not answered)

The IGF2BP2/HMGA2/FOSL1 Axis Controls Cell Plasticity and Therapy Resistance in Neuroblastoma

Tian He[1, 2, #], Jia Shi [1, 2, #], Qichen Liu[1, 2], Kai Chen [1, 2], Qianqian Chen[1, 2], Yujie Tang[3, *], Cheng Cheng[1, 2, *], and Zhixiang Wu [1, 2, *]

Affiliations

1 Department of Pediatric Surgery, Xinhua Hospital, School of Medicine, Shanghai Jiaotong University, Shanghai, 200092, China.

2 Division of Pediatric Oncology, Shanghai Institute of Pediatric Research, Shanghai, 200092, China.

3 Key Laboratory of Cell Differentiation and Apoptosis of National Ministry of Education, Shanghai Key Laboratory of Reproductive Medicine, Department of Histoembryology, Genetics and Developmental Biology, Shanghai Jiao Tong University School of Medicine, Shanghai, 200025, P. R. China.

Correspondence: Yujie Tang, yujietang@shsmu.edu.cn, Cheng Cheng, chengcheng@xinhuamed.com.cn and Zhixiang Wu, wuzhixiang@xinhuamed.com.cn

#These authors contribute equally to the work

Abstract

Adrenergic-to-mesenchymal (ADRN-to-MES) cell-state plasticity is increasingly recognized as a key driver of malignant progression, therapeutic resistance and relapse in high-risk neuroblastoma; however, the mechanisms that govern transition toward and maintenance of the MES state remain incompletely defined. By integrating transcriptomic, proteomic, chromatin-accessibility, and super-enhancer profiling, we identified HMGA2 as a MES-enriched regulator of neuroblastoma cell state. HMGA2 was required to maintain MES-associated chromatin accessibility, cisplatin resistance, invasion and migration, and suppression of GD2 expression. At the chromatin level, HMGA2 cooperated with AP-

1/RUNX-associated MES transcriptional regulators, particularly FOSL1, to reinforce super-enhancer-linked MES transcriptional programs. The MES regulatory program was also linked to m6A-dependent post-transcriptional control: the m6A reader IGF2BP2 supported HMGA2 expression and reinforced the HMGA2/FOSL1 axis. Consistently, METTL3-dependent methylation favored HMGA2/FOSL1 expression and MES-state maintenance, whereas ALKBH5-mediated demethylation was associated with a more differentiated state. Pharmacological inhibition of METTL3 with STM2457 reduced MES-associated chromatin activity, sensitized MES cells to cisplatin, and increased GD2 expression. In single-cell and bulk transcriptomic datasets, pretreatment MES enrichment and high IGF2BP2/HMGA2/FOSL1 expression were associated with poor therapeutic response, adverse outcomes, and reduced predicted cisplatin sensitivity. These findings define an m6A-IGF2BP2-HMGA2/FOSL1 regulatory axis that contributes to therapy-resistant MES-state neuroblastoma and nominate epitranscriptomic and transcriptional-state regulation as potential therapeutic vulnerabilities.

Key words

Neuroblastoma, Mesenchymal phenotype, Tumor cell plasticity, HMGA2, RNA m^{6}A modification

Introduction

Tumor heterogeneity results from dynamic interactions between extrinsic microenvironmental pressures and intrinsic cellular factors, the latter encompassing both genetic and epigenetic changes. Among these, epigenetic regulation of cellular state plasticity represents a key dynamic driver of tumor evolution, adaptation, and therapy resistance, serving as a major target for therapeutic intervention. This non-genetic heterogeneity is orchestrated by core lineage-specifying transcription factors (TFs). These TFs recruit epigenetic modifiers to dynamically remodel chromatin accessibility and, within super-enhancer-driven regulatory circuits, facilitate reversible phenotypic switching between distinct cellular states. Such plasticity underlies critical processes like dedifferentiation and epithelial-mesenchymal transition (EMT), which are fundamental to tumor initiation, progression, and metastasis(1).

Neuroblastoma (NB) is the most common extracranial solid tumor in children. Patients with high-risk disease face a poor long-term survival rate of less than 50%, primarily due to therapy resistance, relapse, and metastasis(2). High-risk neuroblastoma is driven by a series of well-characterized genetic alterations that actively foster intratumoral heterogeneity (3, 4). These include primary driver events such as MYCN amplification, segmental chromosomal gains or losses, ALK abnormalities, and aberrant telomere maintenance. Furthermore, secondary mutations—notably involving the RAS-MAPK pathway, the PI3K-mTOR pathway and TP53 are frequently acquired under therapeutic pressure(5).

In addition to genetic evolution, neuroblastoma is now recognized to comprise multiple cellular states, most prominently the adrenergic (ADRN) and mesenchymal (MES) states, which are defined by distinct epigenetic and transcriptional programs (6). The ADRN state is governed by core transcription factors such as PHOX2B and HAND2 and expresses differentiation markers such as TH. By contrast, the MES state is driven by factors including PRRX1 and AP-1 family members and shows elevated expression of genes linked to invasion and resistance, including VIM and YAP1(ref. 7, 8). These programs confer divergent functional phenotypes. MES-state cells show enhanced invasiveness, chemotherapy resistance, and reduced susceptibility to immunotherapy, whereas ADRN-state cells proliferate rapidly, are more chemosensitive, and express higher levels of disialoganglioside GD2, making them more susceptible to GD2-targeted immunotherapy(9-11). Clinically, a high MES signature correlates with poor prognosis, therapy resistance, and relapse(12). The ADRN state can be further subdivided into subtypes with distinct clinical outcomes (13, 14), and each state differentially remodels the tumor microenvironment (15-17).

Critically, the two states can dynamically interconvert. This plasticity is driven by specific stimuli: for example, HRAS mutation(12) or overexpression of MES TFs like PRRX1(7, 18) can promote an ADRN-to-MES switch, which is associated with acquired resistance. Conversely, pharmacological inhibition of epigenetic regulators such as EZH2 can partially reverse the MES phenotype and upregulate the expression of GD2 (10). This dynamic interchange highlights the therapeutic potential of targeting the state transition machinery itself, offering a promising strategy to overcome drug resistance by preventing or reversing the switch to the resilient MES state.

Therefore, identifying the key transcriptional regulators that sustain the therapy-resistant MES state is crucial for developing rational combination strategies. In this study, we identify HMGA2, a chromatin architectural factor highly expressed in malignant tumors(19, 20) , as a central regulator that cooperates with AP-1 family transcription factors to maintain the malignant MES phenotype. We further show that HMGA2 is post-transcriptionally controlled by the m6A reader IGF2BP2, a known stabilizer of HMGA2 mRNA (21-23) , and that this regulatory axis is therapeutically vulnerable to m6A pathway inhibition.

Materials and Methods

Cell Lines and Cell Culture

A panel of neuroblastoma cell lines , SK-N-BE(2), IMR-32, SH-SY5Y, SK-N-SH, SK-N-AS, and SH-EP was employed in this study. All cells were maintained in MEM/F12 medium supplemented with 10% fetal bovine serum (FBS), 100 U/mL penicillin, and 100 μg/mL streptomycin at 37°C in a humidified atmosphere containing 5% CO_2. To generate stable gene-knockdown models, SH-EP and SK-N-AS cells were transduced with lentiviral

particles. Lentiviral vectors were constructed using the TRC2-pLKO-PURO backbone encoding specific shRNA sequences targeting the gene of interest or a non-targeting scramble control shRNA. Transduced cells were subsequently selected with puromycin to establish stable polyclonal populations.

The METTL3 inhibitor STM2457 was purchased from MedChemExpress (MCE, cat. no. HY-134836). The compound was dissolved in dimethyl sulfoxide (DMSO) to prepare a 10 mM stock solution, which was aliquoted and stored at −80°C. For experimental use, STM2457 was diluted in culture medium to a final working concentration of 10 μM. Cells were treated with STM2457 or an equivalent volume of DMSO (vehicle control) for the specified durations.

Single-Cell RNA Sequencing Data Analysis

Single-cell transcriptomic datasets used in this study were obtained from publicly available repositories. Human neuroblastoma data were downloaded from the NCBI Gene Expression Omnibus (GEO) database under accession number GSE137804. Pan-cancer single-cell data were retrieved from the Human Tumor Atlas Consortium (HTAC; https://humantumoratlas.org/publications/hta4_2025_nature-genetics_wenbao-yu).

Raw sequencing data were processed using Cell Ranger software (10x Genomics) for alignment to the GRCh38/hg38 human reference genome, cell barcode identification, and gene expression quantification. Downstream analysis was performed in R using the Seurat package (v4.1.0). Quality control was applied by retaining cells expressing 200–6,000 genes with a mitochondrial gene content below 10%. Data were subsequently normalized, highly variable genes were selected, and principal component analysis (PCA) was performed for linear dimensionality reduction. Batch effects across samples were mitigated using the Harmony algorithm. Cell clustering was conducted with the FindNeighbors and FindClusters functions, and clusters were visualized in two dimensions using UMAP. Cell type annotation was based on differentially expressed marker genes cross-referenced against published literature.

To assess functional heterogeneity across cell subpopulations, predefined gene signature sets were scored at the single-cell level using the AddModuleScore function in Seurat.

Western Blotting

Cells were lysed in RIPA buffer supplemented with protease inhibitors to obtain total protein lysates. Protein concentrations were determined by the BCA assay. Equal protein amounts (20–30 μg per lane) were resolved by SDS-PAGE and transferred onto PVDF membranes. Membranes were blocked with 5% non-fat skim milk in TBST for 1 h at room temperature, then incubated with primary antibodies overnight at 4°C. After three washes with TBST,

membranes were incubated with HRP-conjugated species-appropriate secondary antibodies for 1 h at room temperature. Protein bands were detected using an enhanced chemiluminescence (ECL) substrate and visualized with a chemiluminescence imaging system. A full list of primary antibodies used is provided in Supplementary Table S1.

Quantitative Real-Time PCR (RT-qPCR)

Total RNA was extracted from cells using TRIzol reagent (Invitrogen) according to the manufacturer's instructions. RNA concentration and purity were assessed using a NanoDrop spectrophotometer. A total of 1 μg of RNA was reverse-transcribed into cDNA using a commercial reverse transcription kit. RT-qPCR was performed on a real-time PCR instrument using SYBR Green Premix under the following thermal cycling conditions: initial denaturation at 95°C for 30 s, followed by 40 cycles of denaturation at 95°C for 5 s and annealing/extension at 60°C for 30 s. All reactions were performed in technical triplicate. Relative gene expression was calculated using the $2^{-\Delta\Delta Ct}$ method with GAPDH as the internal reference gene. Primer sequences are listed in Supplementary Table S2.

CUT&Tag and ATAC-seq

1. Experimental Procedures

ATAC-seq: Chromatin accessibility profiling was performed using the Yeason ATAC-seq kit (cat. no. 12208ES). Briefly, 1–10 × 10^4 viable cells were harvested and incubated with Tn5 transposase at 37°C to simultaneously fragment open chromatin and insert sequencing adapters. Libraries were constructed, and fragments below 700 bp were size-selected using AMPure XP beads. Paired-end 150 bp (PE150) sequencing was performed on an Illumina NovaSeq 6000 platform.

CUT&Tag: Chromatin immunoprecipitation-based profiling was conducted using the Yeason CUT&Tag kit (cat. no. 12592ES). Approximately 1 × 10^5 cells were immobilized on Concanavalin A-coated magnetic beads. Cells were sequentially incubated with the primary antibody targeting the protein of interest, followed by a secondary antibody and a pA-Tn5 fusion protein. Guided by the antibody, pA-Tn5 performed in situ DNA cleavage and adapter insertion at target genomic loci. After PCR amplification, PE150 sequencing was conducted on the Illumina NovaSeq 6000 platform.

2. Bioinformatics Analysis

Raw sequencing data quality was assessed using FastQC (v0.11.9). Adapter trimming and quality filtering (quality score < 15) were performed with fastp (v0.23.2). Clean reads were aligned to the GRCh38/hg38 reference genome using Bowtie2 (v2.4.5). For ATAC-seq data, mitochondrial reads were removed prior to alignment using SAMtools. Resulting SAM files were converted to sorted BAM files, and PCR duplicates were removed using SAMtools

rmdup (v1.15). Reads with a mapping quality score (MAPQ) ≥ 30 were retained for downstream analysis.

Peak calling: Significant peaks were identified using MACS2 (v2.2.7.1) with parameters: --nomodel --shift -100 --extsize 200. Peaks were called at a false discovery rate (FDR) < 0.05 after Benjamini–Hochberg correction. Genomic annotation of peaks was performed using the ChIPseeker R package (v1.34.1).

Enhancer and super-enhancer identification: Enhancers and super-enhancers were identified from ATAC-seq peak files using the ROSE2 algorithm with default parameters. Peaks within 3 kb of a transcription start site (TSS) were excluded to eliminate promoter-associated regions.

Signal visualization: Read-coverage tracks in bigWig format were generated from deduplicated BAM files using bamCoverage from deepTools2 (v3.5.1) with parameters --normalizeUsing RPKM --binSize 10. Aggregate signal heatmaps and profile plots over regions of interest were generated using computeMatrix and plotHeatmap/plotProfile from the same package.

Cell Viability Assays

1. CCK-8 Assay

Cells were seeded into 96-well plates at the appropriate density. After the indicated treatment, 10 μL of CCK-8 reagent (Beyotime, cat. no. C0039) was added to each well and cells were incubated for 1–4 h. Absorbance was measured at 450 nm using a microplate reader. All experiments were independently repeated three times.

2. EdU Flow Cytometry Assay

Cell proliferation was assessed using the EdU Cell Proliferation Kit (RiboBio, cat. no. C10310-3). Cells were incubated with 10 μM EdU for 2 h at 37°C. Following fixation and permeabilization, incorporated EdU was conjugated to an Alexa Fluor 488 fluorophore via copper-catalyzed azide–alkyne cycloaddition (Click chemistry). The percentage of EdU-positive cells was quantified by flow cytometry using a CytoFLEX S instrument (Beckman Coulter). All experiments were independently repeated three times.

Transwell and Wound-Healing Assays

1. Invasion Assay

Cells were seeded into the upper chamber of Transwell inserts pre-coated with Matrigel. The lower chamber was filled with medium containing 20% FBS as a chemoattractant. After 48 h of incubation, invasive cells on the lower surface of the membrane were fixed, stained with

crystal violet, and counted under a light microscope.

2. Migration Assay

The migration assay was performed using the same protocol as the invasion assay, with the exception that Transwell inserts were not pre-coated with Matrigel and the incubation period was reduced to 24 h. All experiments were independently repeated three times.

3. Wound-Healing Assay

Cells grown to confluence were scratched with a sterile pipette tip to create a uniform wound. Culture medium was replaced with serum-free medium immediately after scratching. Phase-contrast images of the wound were captured at 0 h and 24 h (or 48 h). The wound closure area was quantified using ImageJ software, and the healing rate was calculated. All experiments were independently repeated three times.

Statistical Analysis

All quantitative data are presented as mean ± standard deviation (SD). Comparisons between two groups were performed using an unpaired, two-tailed Student's t-test. For comparisons among three or more groups, one-way analysis of variance (ANOVA) followed by Tukey's post hoc test was applied. Statistical analyses and graphing were performed using GraphPad Prism 9.0. Statistical significance was defined as: *$p < 0.05$, **$p < 0.01$, ***$p < 0.001$, and ****$p < 0.0001$. All biological experiments were independently repeated at least three times.

Bioinformatics analyses were performed in R (v4.1.0) within the RStudio environment. Differential gene expression analysis of RNA-seq data was conducted using DESeq2 (v1.34.0); the limma package (v3.50.3) was applied to microarray or pre-normalized count data. Single-cell RNA-seq data processing, including quality control, dimensionality reduction, clustering, and cell-type annotation, was performed using Seurat (v4.1.0). Gene set enrichment and variation analysis were conducted using the GSVA package (v1.42.0). Drug sensitivity prediction based on genomic features was accomplished with oncoPredict (v0.2). Survival analysis, including Kaplan–Meier curve generation and log-rank testing, was performed using the survival (v3.2-13) and survminer (v0.4.9) packages. ChIP-seq peak annotation and visualization were carried out using ChIPseeker (v1.30.3). Data visualization and processing were supported by ggplot2 (v3.3.5), pheatmap (v1.0.12), and clusterProfiler (v4.2.2).

Results

Multi-omics Profiling Identifies HMGA2 as a MES-Associated Transcriptional Regulator in Neuroblastoma

To characterize the molecular differences between ADRN and MES cellular states, we re-analyzed public multi-omics datasets from neuroblastoma cell lines, including transcriptomic data from DEPMAP, proteomic data from Cell Passport, and H3K27ac ChIP-seq data from GSE90683. Principal component analysis (PCA) clearly separated the two states across all molecular layers (Supplementary Fig. S1A). Consistently, H3K27ac ChIP-seq signals at super-enhancer (SE) regions displayed state-specific patterns (Supplementary Fig. S1B), and volcano plots of transcriptomic data highlighted HMGA2 as one of the most significantly differentially expressed genes (Supplementary Fig. S1C).

By intersecting transcriptomic (81 differential TFs), proteomic (34 differential TFs), and ChIP-seq (596 differentially bound TF-target genes) datasets, we identified eight TFs that were consistently altered across all three layers. HMGA2, FOSL1, and FOSL2 were preferentially expressed in MES cells, whereas MYT1 represented an ADRN-associated candidate (Fig. 1A). Among the MES-associated candidates, HMGA2 was the only TF that also overlapped with SE-associated TFs shared across three MES cell lines (Fig. 1B). H3K27ac density at selected loci further supported this state specificity: HMGA2 showed stronger signal in MES cells, whereas PHOX2A and PHOX2B were enriched in ADRN cells (Fig. 1C). We then examined candidate expression across transcriptomic and proteomic layers. Heatmaps of the top upregulated and downregulated TFs separated MES from ADRN states at the transcriptomic level (Fig. 1D), with similar patterns at the protein level (Supplementary Fig. S1D). Correlation analysis further showed stronger co-expression among TFs belonging to the same state, including a positive correlation between HMGA2 and FOSL1 (Fig. 1E), and comparable trends were observed in proteomic data (Supplementary Fig. S1E). Finally, validation in neuroblastoma cell lines confirmed that HMGA2 was selectively expressed in MES-type cells such as SH-EP and SK-N-AS, where it was co-expressed with established MES markers at both mRNA and protein levels (Fig. 1F-G). HMGA2 expression was also higher in MES-state cell lines and MES-enriched clinical samples than in ADRN counterparts in the DepMap and SEQC datasets (Fig. 1H).

Having identified candidate MES-associated transcriptional regulators through integrative multi-omics analysis, we next asked whether the neuroblastoma cell models used in this study faithfully reflected the expected ADRN and MES phenotypic states. Immunofluorescence analysis showed that GD2 was highly expressed in ADRN-type cell lines (e.g., SK-N-BE(2), IMR32, SH-SY5Y) but barely detectable in MES-type cells (e.g., SK-N-AS, SH-EP) (Supplementary Fig. S2A). Flow cytometry further revealed that ADRN-like clones had a higher proportion of GD2-positive cells than MES-like clones (Supplementary Fig. S2E).

qPCR analysis of clones derived from the mixed SK-N-SH cell line confirmed that MES-like clones expressed higher levels of HMGA2 and lower levels of PHOX2B compared to ADRN-like clones (Supplementary Fig. S2B). In terms of cellular phenotype, MES-like clones exhibited increased resistance to cisplatin (IC50 = 18.75 μM) relative to ADRN-like clones (IC50 = 6.95 μM) (Supplementary Fig. S2C), and demonstrated significantly enhanced migratory capacity in wound healing assays ($p < 0.0001$, Supplementary Fig. S2D). Collectively, these results indicate that the MES state is associated with reduced GD2 expression, increased chemoresistance, and heightened migratory ability.

Consistent with these phenotypic differences, GSVA was performed using KEGG pathway gene sets to generate a pathway-level activity score matrix for DEPMAP ADRN and MES cell lines. Limma-based differential analysis of these GSVA scores revealed distinct functional programs associated with each state: MES cells showed higher activity scores for pathways related to focal adhesion and ECM-receptor interaction, whereas ADRN cells showed higher activity scores for DNA repair and DNA replication pathways (Supplementary Fig. S2J). Together with the multi-omics prioritization of HMGA2, these phenotypic and pathway-level features supported HMGA2 as a candidate regulator of the MES-associated malignant program.

HMGA2 Sustains the MES Phenotype and Regulates ADRN-MES Cell-State Plasticity

To investigate the functional necessity of HMGA2 in MES state maintenance, we performed gain-of-function and loss-of-function experiments. Knockdown of HMGA2 in two MES-type cell lines (SK-N-AS and SH-EP) significantly downregulated core MES markers (e.g., PRRX1, VIM) while upregulating the ADRN marker PHOX2B (Fig. 2A). Conversely, ectopic HMGA2 expression in ADRN cells (SH-SY5Y and BE2) induced partial MES-like reprogramming, as evidenced by elevated MES markers VIM (Fig. 2B). RT-qPCR validation confirmed these bidirectional regulatory effects at the transcript level (Fig. 2C).

Functional interrogation revealed pleiotropic roles of HMGA2 in maintaining MES-associated malignancy. HMGA2 depletion significantly reduced the half-maximal inhibitory concentration (IC50) of cisplatin in both MES cell lines (Resistance Index, RI = $\log_2$(IC50_KD/IC50_ctrl) < –1; Fig. 2D), impaired migration and invasion capacities as assessed by wound healing and Transwell assays (Fig. 2E), and de-repressed GD2 surface antigen expression, as shown by immunofluorescence (Fig. 2F) and flow cytometry (Supplementary Fig. S2G). Moreover, HMGA2 knockdown attenuated the MES transcriptional program and induced a shift toward ADRN phenotype, as demonstrated by single-sample Gene Set Variation Analysis (ssGSEA) using an ADRN-MES signature (Fig. 2G). Consistently, pathway-level GSVA/limma analysis showed that HMGA2 knockdown decreased MES-associated pathway activity, including PI3K-Akt signaling, focal adhesion, and ECM-receptor interaction, while increasing ADRN-associated pathway activity, including

spliceosome, DNA replication, and mismatch repair (Fig. 2H; Supplementary Fig. S2K).

Reciprocal experiments in ADRN cells showed that HMGA2 overexpression conferred enhanced cisplatin resistance (Supplementary Fig. S2H). To further characterize the transcriptional consequences of HMGA2 overexpression, we performed RNA-seq in the MYCN-amplified ADRN cell line SK-N-BE(2). ssGSEA analysis using predefined gene sets representing different cellular states revealed that HMGA2 overexpression significantly increased enrichment scores for proliferative subgroups (cyc_CHC and cyc_SN), while decreasing scores for non-proliferative subgroups (noncyc_CHC, noncyc_SN and SCPs) (Supplementary Fig. S2I). Concurrently, gene sets representing early developmental lineage states, including neural tube (NTs) and epithelial-mesenchymal transition-associated neural crest cells (EMT_NCCs), were consistently upregulated (Supplementary Fig. S2I). These data indicate that HMGA2 drives MYCN-amplified ADRN cells toward a more undifferentiated, migratory neural crest-like state.

Collectively, these results demonstrate that HMGA2 is required for MES-state maintenance and can promote partial MES-like reprogramming in ADRN cells, supporting a central role for HMGA2 in regulating ADRN-MES plasticity in neuroblastoma.

HMGA2 Maintains MES-specific Chromatin Accessibility and Facilitates FOSL1 Recruitment

Because HMGA2 is a chromatin architectural factor, we first examined whether it occupies accessible regulatory regions in MES-state neuroblastoma cells. Genome-wide CUT&Tag profiling in SH-EP and SK-N-AS cells showed that HMGA2 signals were predominantly localized to open chromatin regions (Fig. 3A). Genomic annotation further revealed enrichment of HMGA2 binding at promoters and distal intergenic regions, and 64% of HMGA2 peaks overlapped with ATAC-seq peaks (OR = 55.6, $p < 2.2 \times 10^{-16}$), supporting a strong preference for accessible chromatin (Fig. 3B). Unsupervised clustering of H3K27ac signals at HMGA2-bound regions identified chromatin modules associated with cell-matrix adhesion, embryonic development, and basal cellular functions (Supplementary Fig. S3A-B), suggesting that HMGA2 occupies both MES-associated regulatory elements and broader active chromatin regions.

We then tested whether HMGA2 is required to maintain the MES-associated chromatin landscape. HMGA2 knockdown caused a broad reduction of H3K27ac signals at promoters and enhancers, accompanied by decreased MES enrichment scores and increased ADRN scores (Fig. 3C). Pathway analysis of regions with reduced H3K27ac signals highlighted MES-associated programs, including PI3K-Akt signaling and focal adhesion (Fig. 3D). ATAC-seq-based analyses further supported a loss of MES-specific chromatin accessibility after HMGA2 depletion (Supplementary Fig. S3C-D). Representative IGV tracks at MES-

associated loci further supported these genome-wide observations, showing reduced chromatin accessibility, H3K27ac enrichment, and/or FOSL1 occupancy at HMGA2-associated regulatory regions after HMGA2 depletion (Fig. 3H; Supplementary Fig. S3E).

To identify transcriptional regulators acting within HMGA2-associated chromatin regions, we performed motif and CUT&Tag-based co-occupancy analyses. HMGA2-bound regions were enriched for AP-1 family motifs, including FOSL1, FOSL2, and JUNB, as well as RUNX motifs (Fig. 3E). Consistently, FOSL1, JUNB, and RUNX2 signals were enriched around HMGA2 binding centers, indicating that these MES-associated transcription factors occupy HMGA2-associated accessible regions (Fig. 3F). TSS-centered signal maps provided additional support for AP-1/RUNX occupancy around promoter-proximal regions (Supplementary Fig. S3F). When HMGA2 was depleted, FOSL1 occupancy was markedly reduced at HMGA2-bound regions and showed a similar reduction around TSS-proximal regions (Fig. 3G; Supplementary Fig. S3G). In parallel, JUNB CUT&Tag analysis comparing control and HMGA2-knockdown cells showed a weaker and more selective change in JUNB occupancy at HMGA2-bound and TSS-proximal regions, with genes associated with differential JUNB peaks remaining enriched for MES-related pathways (Supplementary Fig. S4A-B). Co-immunoprecipitation analyses supported interactions within the AP-1-associated regulatory network, including FOSL1-JUNB interaction, while HMGA2-FOSL1 association was not robust under stringent conditions (Supplementary Fig. S3H-I). Thus, FOSL1 showed the clearest HMGA2-dependent chromatin occupancy in this dataset, whereas JUNB and RUNX2 appear to function as additional components of a broader MES-associated transcription factor network.

Additional analyses showed that HMGA2 depletion was accompanied by increased KDM1A occupancy at selected regulatory regions suggesting that chromatin-repressive regulators may contribute to the broader response to HMGA2 loss (Supplementary Fig. S4C-F).

Together, these data indicate that HMGA2 maintains an accessible MES-associated chromatin landscape and preferentially supports FOSL1 recruitment, positioning FOSL1 as a major HMGA2-dependent effector within the MES transcriptional network.

The HMGA2-FOSL1 Regulatory Module Reinforces MES Malignancy through Super-Enhancer-Linked Transcriptional Amplification

Because FOSL1 showed the strongest HMGA2-dependent chromatin occupancy, we next examined whether HMGA2 and FOSL1 cooperate at super-enhancer-linked regulatory regions to sustain the MES malignant program. Genome-wide co-occupancy analysis showed that a substantial fraction of HMGA2 peaks overlapped with FOSL1 peaks (Fig. 4A). Genes co-bound by HMGA2 and FOSL1 were enriched in PI3K-Akt signaling, focal adhesion, and other MES-associated pathways (Fig. 4B). Boundary profiles further showed enrichment of

both HMGA2 and FOSL1 around super-enhancer centers, and both factors displayed higher enrichment at super-enhancers than at typical enhancers (Fig. 4C-D). Additional SE-centered profiles supported the enrichment of HMGA2, FOSL1, JUNB, and RUNX2 at SE-associated regulatory regions (Supplementary Fig. S5A).

We then examined regulatory interactions within this circuitry. HMGA2 occupancy was detected at regulatory regions of FOSL1, JUNB, and RUNX2 by ChIP-qPCR (Fig. 4E), and HMGA2 knockdown reduced expression of these MES-associated transcription factors, as shown by RT-qPCR (Fig. 4F). Integrative IGV and Hi-C loop visualization at the VIM-associated SE region further showed HMGA2, FOSL1, JUNB, and RUNX2 occupancy near SE-linked regulatory elements and chromatin-loop interactions connecting these regulatory regions to the VIM locus (Supplementary Fig. S5B). Spatial motif analysis revealed preferred spacing between FOSL1 and JUNB motifs, consistent with AP-1 heterodimer binding architecture (Supplementary Fig. S5C). These findings support a regulatory module in which HMGA2 and FOSL1 act at SE-associated chromatin regions within a broader AP-1/RUNX transcriptional network.

To test the functional role of FOSL1 in this module, we examined state-associated transcriptional programs after FOSL1 knockdown. FOSL1 depletion reduced MES signature scores and increased ADRN scores, supporting its role as a downstream effector of HMGA2-dependent chromatin regulation (Fig. 4G). Consistent with a role for FOSL1 in maintaining active MES regulatory regions, FOSL1 knockdown reduced H3K27ac signals at MES-associated regulatory regions (Supplementary Fig. S5D). Knockdown efficiency and AP-1/RUNX network perturbation were confirmed at the protein level after FOSL1, JUNB, or RUNX2 depletion (Supplementary Fig. S5E). JUNB and RUNX2 perturbation produced more partial effects on MES/ADRN state scores, and transcriptomic read-count analysis further showed compensatory or coordinated changes among AP-1 family members after FOSL1 or JUNB knockdown (Supplementary Fig. S5F-G).

We next asked whether the HMGA2-FOSL1 module converges on downstream pathways that mediate MES-associated malignant phenotypes. Shared transcriptional changes after HMGA2 and FOSL1 depletion converged on PI3K-Akt signaling and focal adhesion pathways (Fig. 4H). Consistently, activation of PI3K-Akt signaling increased MES scores while reducing ADRN scores, supporting this pathway as one downstream component of the MES regulatory program (Supplementary Fig. S5H).

Functionally, knockdown of FOSL1, JUNB, or RUNX2 impaired migration and invasion, increased GD2 expression, and enhanced cisplatin sensitivity (Fig. 4I-K). These findings indicate that HMGA2-associated AP-1/RUNX circuitry, centered on FOSL1, sustains MES-associated malignancy and therapy resistance. Collectively, the chromatin and functional data support a model in which HMGA2 maintains accessible MES regulatory regions, facilitates

FOSL1 recruitment, and cooperates with FOSL1 at super-enhancer-linked regulatory hubs to amplify the MES malignant program.

IGF2BP2 Sustains HMGA2 Expression

Having established HMGA2-FOSL1 as a chromatin-linked MES regulatory module, we next asked how HMGA2 expression is maintained in MES cells. Because RNA-binding proteins can regulate HMGA2 mRNA, we compared RBP expression between ADRN and MES states and identified IGF2BP2 as a MES-enriched RBP (Fig. 5A), with expression strongly correlated with HMGA2 levels (Fig. 5B). Functionally, IGF2BP2 knockdown reduced HMGA2 and downstream MES markers, including FOSL1 (Fig. 5C-E; Supplementary Fig. S6A). RNA-seq further showed that IGF2BP2 silencing decreased MES signature scores, whereas genes upregulated after IGF2BP2 depletion were enriched for ADRN-associated processes, including DNA replication and mismatch repair (Fig. 5F; Supplementary Fig. S6C). Phenotypically, IGF2BP2 depletion attenuated drug resistance, invasion, and migration while increasing GD2 expression (Fig. 5G-I). HMGA2 occupancy at the IGF2BP2 regulatory region, together with reduced IGF2BP2 expression after HMGA2 perturbation, suggested a positive feedback relationship between HMGA2 and IGF2BP2 (Supplementary Fig. S6B). Consistently, the IGF2BP2 inhibitor CWI12 synergized with cisplatin, suppressed invasion and migration, modestly increased GD2 mean fluorescence intensity, and downregulated HMGA2 and other MES markers (Supplementary Fig. S6D-G). These data support a model in which IGF2BP2 helps maintain the HMGA2/FOSL1-associated MES state.

RNA m6A Modification Modulates the IGF2BP2/HMGA2 Axis in MES Maintenance

Because IGF2BP2 often acts through m6A-dependent RNA regulation, we next examined whether m6A modification contributes to HMGA2 expression and MES-state maintenance. Single-cell and bulk transcriptomic analyses showed higher expression of the m6A eraser genes ALKBH5 and FTO in more differentiated ADRN or chromaffin-like states, whereas MES cells showed relatively higher METTL3 and IGF2BP2 expression (Fig. 6A-D). METTL3 knockdown or ALKBH5 overexpression reduced HMGA2 and FOSL1 expression, together with other AP-1 family members, supporting a role for m6A regulation in maintaining the HMGA2-FOSL1 axis (Fig. 6E). Integrative analysis of public m6A-RIP data from neural crest cells and SK-N-BE(2) cells identified HMGA2 as a candidate m6A-regulated transcript within MES-associated gene sets (Fig. 6G; Supplementary Fig. S6H).

To further explore the molecular mechanism, we examined m6A modification of HMGA2 mRNA. IGV visualization of public m6A-RIP data revealed enriched signals in the coding region of HMGA2 in ADRN and neural crest cells (Fig. 6G). Putative m6A sites within HMGA2 were predicted by online tools, and meRIP-qPCR showed that ALKBH5 overexpression reduced m6A enrichment at the HMGA2 transcript (Fig. 6H). Moreover,

ALKBH5 or IGF2BP2 knockdown shortened the half-life of HMGA2 mRNA, consistent with a model in which m6A modification and IGF2BP2 contribute to HMGA2 transcript stability (Fig. 6I). These data support m6A-dependent post-transcriptional regulation of HMGA2, although transcriptome-wide IGF2BP2 binding will be needed to map direct IGF2BP2 targets comprehensively.

We next asked whether perturbing m6A writing activity was sufficient to remodel MES-associated chromatin and transcriptional programs. Treatment of MES cells with the METTL3 inhibitor STM2457 reduced H3K27ac signals, and the regions with decreased H3K27ac were enriched in MES-associated pathways, including focal adhesion (Fig. 6J). Transcriptomic analysis further showed that STM2457 increased ADRN scores while decreasing MES scores and MES-associated KEGG pathways (Fig. 6K; Supplementary Fig. S7H). Consistently, western blotting confirmed that STM2457 reduced the expression of MES markers (Fig. 6F).

Both STM2457 treatment and METTL3 knockdown reduced poor-prognosis gene sets, including the Yuan_Trans signature (a transcriptional program associated with adverse outcome; Yuan et al., 2022) and the Bexell_MES signature (a MES-associated gene set; Bexell et al., 2022) (Supplementary Fig. S7I). Genetic perturbation of m6A regulators also recapitulated aspects of the MES-to-ADRN phenotypic switch. METTL3 knockdown or ALKBH5 overexpression in MES cells increased cisplatin sensitivity, whereas ALKBH5 depletion in SK-N-BE(2) cells enhanced drug resistance (Supplementary Fig. S7A). ALKBH5 knockdown in ADRN cells reduced GD2 expression and promoted migration and invasion, opposite to the effects observed after METTL3 knockdown (Supplementary Fig. S7B-D). Pharmacological inhibition of METTL3 with STM2457 mirrored these phenotypic changes by increasing cisplatin sensitivity, impairing migration, and elevating GD2 expression in MES cells (Fig. 6L; Supplementary Fig. S7E-F).

Collectively, these data support a model in which m6A regulatory balance contributes to HMGA2 expression and MES-state maintenance, with METTL3 activity favoring the HMGA2-FOSL1 program and ALKBH5 activity opposing this state.

Clinical Associations of the MES Phenotype and Predicted Therapeutic Response

To connect these experimental findings with clinical disease, we first examined key molecules in paired primary and recurrent neuroblastoma tissues by immunohistochemistry. Recurrent tumors showed a staining pattern consistent with MES enrichment, including increased HMGA2 and PRRX1 and reduced ALKBH5 and GD2 expression (Fig. 7A).

Given that the MES phenotype has been characterized in the longitudinal single-cell dataset, we next re-analyzed its association with therapeutic response and clinical outcome. In pretreatment samples, elevated MES scores were associated with adverse events and non-

complete remission, whereas this difference was less apparent in post-chemotherapy samples (Fig. 7B). Consistently, the event group showed higher expression of MES markers (Fig. 7D), increased proportions of HMGA2-, FOSL1-, VIM-, and YAP1-positive cells (Supplementary Fig. S8C), and inverse trends for ADRN markers (Supplementary Fig. S8B). The MES subset also expressed HMGA2, IGF2BP2, and FOSL1 (Fig. 7C; Supplementary Fig. S8A).

To evaluate the relationship between MES-state enrichment and predicted chemotherapy response, we used OncoPredict to infer drug sensitivity across SEQC and NRC neuroblastoma cohorts(24). MES-dominant samples and the HMGA2/FOSL1 co-target gene signature were associated with reduced predicted sensitivity to frontline neuroblastoma agents, including cisplatin, doxorubicin, and vincristine (Fig. 7E; Supplementary Fig. S8D-E). High expression of MES-related regulators, including IGF2BP2, HMGA2, and FOSL1, was also associated with reduced predicted cisplatin sensitivity, whereas elevated ALKBH5 and FTO expression showed the opposite trend (Fig. 7F; Supplementary Fig. S8F). Resistant samples had higher HMGA2/FOSL1 co-target gene-set scores than sensitive samples (Fig. 7G). Kaplan-Meier analyses further showed poorer survival in MES/MYCN-amplified groups (Supplementary Fig. S8G). These findings link the HMGA2/FOSL1-associated MES program to adverse clinical features and predicted drug resistance.

Discussion

Despite advances in multimodal therapy, more than 20% of patients with high-risk neuroblastoma (NB) still experience disease progression driven by metastasis, relapse, or therapeutic resistance (25). Emerging evidence implicates lineage plasticity, particularly adrenergic-to-mesenchymal transition (AMT), as a critical determinant of adverse outcomes. Single-cell analyses consistently reveal enrichment of MES signature genes and expansion of MES-like subpopulations in refractory or recurrent tumors, suggesting that this cellular reprogramming represents a fundamental mechanism underlying treatment failure. However, the transcriptional circuitry that stabilizes the MES state remains incompletely understood.

Through integrative multi-omics analysis of NB cell-line datasets, including ChIP-seq, RNA-seq, and proteomics, we identified HMGA2 as a central regulator of the MES phenotype. Functional perturbation showed that HMGA2 loss suppressed the MES transcriptional program and reactivated a subset of ADRN markers, supporting its role in cell-state control. This finding is consistent with reports linking HMGA2 to tumor progression and lineage plasticity in other cancers (22, 26-29). Genomic occupancy analyses further showed that HMGA2-bound regions were enriched for AP-1 family and RUNX motifs and were co-occupied by MES-associated transcription factors. Among these candidates, FOSL1 showed the strongest HMGA2-dependent chromatin occupancy and functional synergy, whereas JUNB and RUNX2 also contributed to MES-associated malignant phenotypes. These findings support a hierarchical model in which HMGA2 reinforces a FOSL1-centered core program

while also engaging a broader AP-1/RUNX-associated MES regulatory network.

The chromatin-level data also link the HMGA2-FOSL1 module to super-enhancer regulation. Both factors were enriched at super-enhancers, and shared HMGA2/FOSL1 target genes converged on PI3K-AKT and focal adhesion pathways. Together with evidence that PI3K activation can drive ADRN-to-MES reprogramming(30-32) , these findings support a model in which the HMGA2-FOSL1 axis occupies super-enhancer-linked regulatory hubs and activates gene networks that stabilize the MES state and promote therapy resistance. The current data support HMGA2 as a chromatin-associated architectural regulator; additional experiments assessing chromatin accessibility and HMGA2 occupancy after FOSL1 depletion would further clarify the hierarchy between HMGA2 and FOSL1.

We further linked this chromatin-centered program to post-transcriptional regulation. IGF2BP2 supported HMGA2 expression and MES-associated phenotypes, while perturbation of METTL3 or ALKBH5 shifted HMGA2/FOSL1 expression and state-associated programs in opposite directions. These findings suggest that m6A-dependent RNA regulation helps stabilize the HMGA2/FOSL1 axis, with METTL3 favoring the MES state and ALKBH5 opposing it. Pharmacological inhibition of METTL3 with STM2457(33) suppressed the HMGA2/FOSL1-associated program and modulated cellular plasticity, consistent with reports that METTL3 inhibition promotes NB differentiation (34). Although these results highlight therapeutic potential, clinical translation will require a deeper understanding of m6A modifier tissue specificity, direct IGF2BP2 RNA targets, and possible off-target effects.

At the clinical level, MES enrichment and the HMGA2/FOSL1-associated program were associated with adverse outcome and reduced predicted sensitivity to frontline chemotherapeutic agents. These analyses extend previous observations that MES signatures are associated with poor prognosis by connecting the MES state to the experimentally defined IGF2BP2-HMGA2-FOSL1 regulatory axis. However, the clinical and drug-sensitivity analyses remain predictive and correlative. They support the clinical relevance of the MES program but do not by themselves prove that targeting this axis restores drug sensitivity in patients. Further validation in in vivo models and clinically annotated therapeutic-response cohorts will therefore be required.

In summary, this study identifies HMGA2 as a chromatin-associated regulator of MES-state neuroblastoma and connects it to FOSL1-dependent transcriptional amplification, m6A/IGF2BP2-mediated post-transcriptional regulation, and predicted therapeutic resistance. These findings support a model in which chromatin-state control and RNA methylation cooperate to stabilize the therapy-resistant MES program, providing a rationale for targeting HMGA2 stability, FOSL1-centered circuitry, or upstream m6A regulation in high-risk neuroblastoma.

Reference

1. Pérez-González A, Bévant K, Blanpain C. Cancer cell plasticity during tumor progression, metastasis and response to therapy. Nat Cancer. 2023;4(8):1063-82.
2. Matthay KK, Maris JM, Schleiermacher G, Nakagawara A, Mackall CL, Diller L, et al. Neuroblastoma. Nat Rev Dis Primers. 2016;2:16078.
3. Bosse KR, Giudice AM, Lane MV, McIntyre B, Schürch PM, Pascual-Pasto G, et al. Serial Profiling of Circulating Tumor DNA Identifies Dynamic Evolution of Clinically Actionable Genomic Alterations in High-Risk Neuroblastoma. Cancer Discov. 2022;12(12):2800-19.
4. He XQ, C.; Zhao, Y.; Zou, L.; Zhao, H.; Cheng, C. Gene signatures associated with genomic aberrations predict prognosis in neuroblastoma. Cancer communications (London, England). 2020;40(2-3):105-18.
5. Gundem G, Levine MF, Roberts SS, Cheung IY, Medina-Martínez JS, Feng Y, et al. Clonal evolution during metastatic spread in high-risk neuroblastoma. Nat Genet. 2023;55(6):1022-33.
6. Yuan X, Seneviratne JA, Du S, Xu Y, Chen Y, Jin Q, et al. Single-cell profiling of peripheral neuroblastic tumors identifies an aggressive transitional state that bridges an adrenergic-mesenchymal trajectory. Cell Rep. 2022;41(1):111455.
7. van Groningen T, Koster J, Valentijn LJ, Zwijnenburg DA, Akogul N, Hasselt NE, et al. Neuroblastoma is composed of two super-enhancer-associated differentiation states. Nat Genet. 2017;49(8):1261-6.
8. Boeva V, Louis-Brennetot C, Peltier A, Durand S, Pierre-Eugène C, Raynal V, et al. Heterogeneity of neuroblastoma cell identity defined by transcriptional circuitries. Nat Genet. 2017;49(9):1408-13.
9. Mañas A, Aaltonen K, Andersson N, Hansson K, Adamska A, Seger A, et al. Clinically relevant treatment of PDX models reveals patterns of neuroblastoma chemoresistance. Sci Adv. 2022;8(43):eabq4617.
10. Mabe NW, Huang M, Dalton GN, Alexe G, Schaefer DA, Geraghty AC, et al. Transition to a mesenchymal state in neuroblastoma confers resistance to anti-GD2 antibody via reduced expression of ST8SIA1. Nat Cancer. 2022;3(8):976-93.
11. Sengupta S, Das S, Crespo AC, Cornel AM, Patel AG, Mahadevan NR, et al. Mesenchymal and adrenergic cell lineage states in neuroblastoma possess distinct immunogenic phenotypes. Nat Cancer. 2022;3(10):1228-46.
12. Gartlgruber M, Sharma AK, Quintero A, Dreidax D, Jansky S, Park Y-G, et al. Super enhancers define regulatory subtypes and cell identity in neuroblastoma. Nat Cancer. 2021;2(1):114-28.
13. Dong R, Yang R, Zhan Y, Lai H-D, Ye C-J, Yao X-Y, et al. Single-Cell Characterization of Malignant Phenotypes and Developmental Trajectories of Adrenal Neuroblastoma. Cancer Cell. 2020;38(5).
14. Yu W, Biyik-Sit R, Uzun Y, Chen C-H, Thadi A, Sussman JH, et al. Longitudinal single-cell multiomic atlas of high-risk neuroblastoma reveals chemotherapy-induced tumor microenvironment rewiring

Nat Genet. 2025;57(5):1142-54.

15. Yang YL, H.; Zheng, D.; Li, X.; Liu, H. Immune microenvironment heterogeneity reveals distinct subtypes in neuroblastoma: insights into prognosis and therapeutic targets. Aging. 2023;15(22):13345-67.
16. Verhoeven BM, Mei S, Olsen TK, Gustafsson K, Valind A, Lindström A, et al. The immune cell atlas of human neuroblastoma. Cell Reports Medicine. 2022;3(6):100657.
17. Wienke J, Visser LL, Kholosy WM, Keller KM, Barisa M, Poon E, et al. Integrative analysis of neuroblastoma by single-cell RNA sequencing identifies the NECTIN2-TIGIT axis as a target for immunotherapy. Cancer Cell. 2023.
18. van Groningen T, Akogul N, Westerhout EM, Chan A, Hasselt NE, Zwijnenburg DA, et al. A NOTCH feed-forward loop drives reprogramming from adrenergic to mesenchymal state in neuroblastoma. Nat Commun. 2019;10(1):1530.
19. Dong J, Wang R, Ren G, Li X, Wang J, Sun Y, et al. HMGA2-FOXL2 Axis Regulates Metastases and Epithelial-to-Mesenchymal Transition of Chemoresistant Gastric Cancer. Clinical cancer research : an official journal of the American Association for Cancer Research. 2017;23(13):3461-73.
20. Wang X, Wang J, Zhao J, Wang H, Chen J, Wu J. HMGA2 facilitates colorectal cancer progression via STAT3-mediated tumor-associated macrophage recruitment. Theranostics. 2022;12(2):963-75.
21. Oliveira-Mateos C, Sánchez-Castillo A, Soler M, Obiols-Guardia A, Piñeyro D, Boque-Sastre R, et al. The transcribed pseudogene RPSAP52 enhances the oncofetal HMGA2-IGF2BP2-RAS axis through LIN28B-dependent and independent let-7 inhibition. Nat Commun. 2019;10(1):3979.
22. Chen R-X, Chen X, Xia L-P, Zhang J-X, Pan Z-Z, Ma X-D, et al. N6-methyladenosine modification of circNSUN2 facilitates cytoplasmic export and stabilizes HMGA2 to promote colorectal liver metastasis. Nat Commun. 2019;10(1):4695.
23. Bai J, Yokomizo-Nakano T, Kubota S, Sun Y, Kanai A, Iimori M, et al. Overexpression of Hmga2 activates Igf2bp2 and remodels transcriptional program of Tet2-deficient stem cells in myeloid transformation. Oncogene. 2021;40(8):1531-41.
24. Maeser D, Gruener RF, Huang RS. oncoPredict: an R package for predicting in vivo or cancer patient drug response and biomarkers from cell line screening data. Brief Bioinform. 2021;22(6).
25. Qiu B, Matthay KK. Advancing therapy for neuroblastoma. Nat Rev Clin Oncol. 2022;19(8):515-33.
26. Song C-Q, Li Y, Mou H, Moore J, Park A, Pomyen Y, et al. Genome-Wide CRISPR Screen Identifies Regulators of Mitogen-Activated Protein Kinase as Suppressors of Liver Tumors in Mice. Gastroenterology. 2017;152(5).
27. Wang Y, Chen Y, Liang J, Jiang M, Zhang T, Wan X, et al. METTL3-mediated m6A modification of HMGA2 mRNA promotes subretinal fibrosis and epithelial-mesenchymal transition. Journal of Molecular Cell Biology. 2023;15(3).
28. Pugh TJ, Morozova O, Attiyeh EF, Asgharzadeh S, Wei JS, Auclair D, et al. The genetic landscape of high-risk neuroblastoma. Nat Genet. 2013;45(3):279-84.
29. Dobersch S, Yamamoto N, Schutter A, Cavender SM, Robertson TM, Kartha N, et al. HMGA2 and protein leucine methylation drive pancreatic cancer lineage plasticity. Nat Commun. 2025;16(1):4866.

30. Mohlin S, Hamidian A, von Stedingk K, Bridges E, Wigerup C, Bexell D, et al. PI3K-mTORC2 but not PI3K-mTORC1 regulates transcription of HIF2A/EPAS1 and vascularization in neuroblastoma. Cancer Res. 2015;75(21):4617-28.
31. Tian X, Xia Y, Gong W, Zhu K, Yang Y, Han Z, et al. PLK4 as a Key Regulator of Neuroblastoma Differentiation and a Promising Therapeutic Target. Int J Biol Sci. 2025;21(11):4979-96.
32. Tian X, Zhou D, Chen L, Tian Y, Zhong B, Cao Y, et al. Polo-like kinase 4 mediates epithelial-mesenchymal transition in neuroblastoma via PI3K/Akt signaling pathway. Cell Death Dis. 2018;9(2):54.
33. Yankova E, Blackaby W, Albertella M, Rak J, De Braekeleer E, Tsagkogeorga G, et al. Small-molecule inhibition of METTL3 as a strategy against myeloid leukaemia. Nature. 2021;593(7860):597-601.
34. Pomaville M, Chennakesavalu M, Wang P, Jiang Z, Sun H-L, Ren P, et al. Small-molecule inhibition of the METTL3/METTL14 complex suppresses neuroblastoma tumor growth and promotes differentiation. Cell Rep. 2024;43(5):114165.

Acknowledgements

Not applicable

Funding

This work was carried out under the National Natural Science Foundation of China (No. 82472715) to Dr. Zhixiang Wu and the National Natural Science Foundation of China (No. 82503961) to Dr. Cheng Cheng.

Ethics approval

All experiments involving human cell lines were performed using established cell lines obtained from authorized sources. The immunohistochemistry validation using paired primary and recurrent neuroblastoma tumor tissues was performed on archived/de-identified specimens from a previously published cohort from our group. No additional patient recruitment or new sample collection was conducted for the present study. This study did not involve animal experiments.

Competing Interests

All authors declare no competing interests.

Authors' Contributions

T.H.: Conceptualization, Methodology, Investigation, Formal analysis, Visualization, Writing - original draft.

J.S.: Methodology, Investigation, Formal analysis, Visualization, Writing - original draft.

Q.L.: Investigation, Data curation, Formal analysis, Visualization.

K.C.: Investigation, Validation, Resources.

Q.C.: Investigation, Validation, Data curation.

Y.T.: Conceptualization, Supervision, Writing - review & editing.

C.C.: Conceptualization, Supervision, Funding acquisition, Writing - review & editing.

Z.W.: Conceptualization, Supervision, Project administration, Funding acquisition, Writing - review & editing.

All authors read and approved the final manuscript.

Data Availability

Data Availability Statement

All data supporting the findings of this study are available within the article and its Supplementary Materials. The single-cell RNA sequencing dataset analyzed in this study is publicly available in the NCBI Gene Expression Omnibus (GEO) repository under accession number GSE137804. Pan-cancer single-cell transcriptomic data were obtained from the Human Tumor Atlas Consortium (HTAC) and are accessible at https://humantumoratlas.org/publications/hta4_2025_nature-genetics_wenbao-yu.

The raw sequencing data generated in this study (ATAC-seq and CUT&Tag) have been deposited in the NCBI GEO repository and are publicly accessible under accession number [GSE######] (to be updated upon acceptance). Bulk RNA-seq data generated in this study are similarly deposited under accession number [GSE, GSE] (to be updated upon acceptance).

All other data, materials, and reagents used in this study are available from the corresponding author upon reasonable request.

Figure Legend

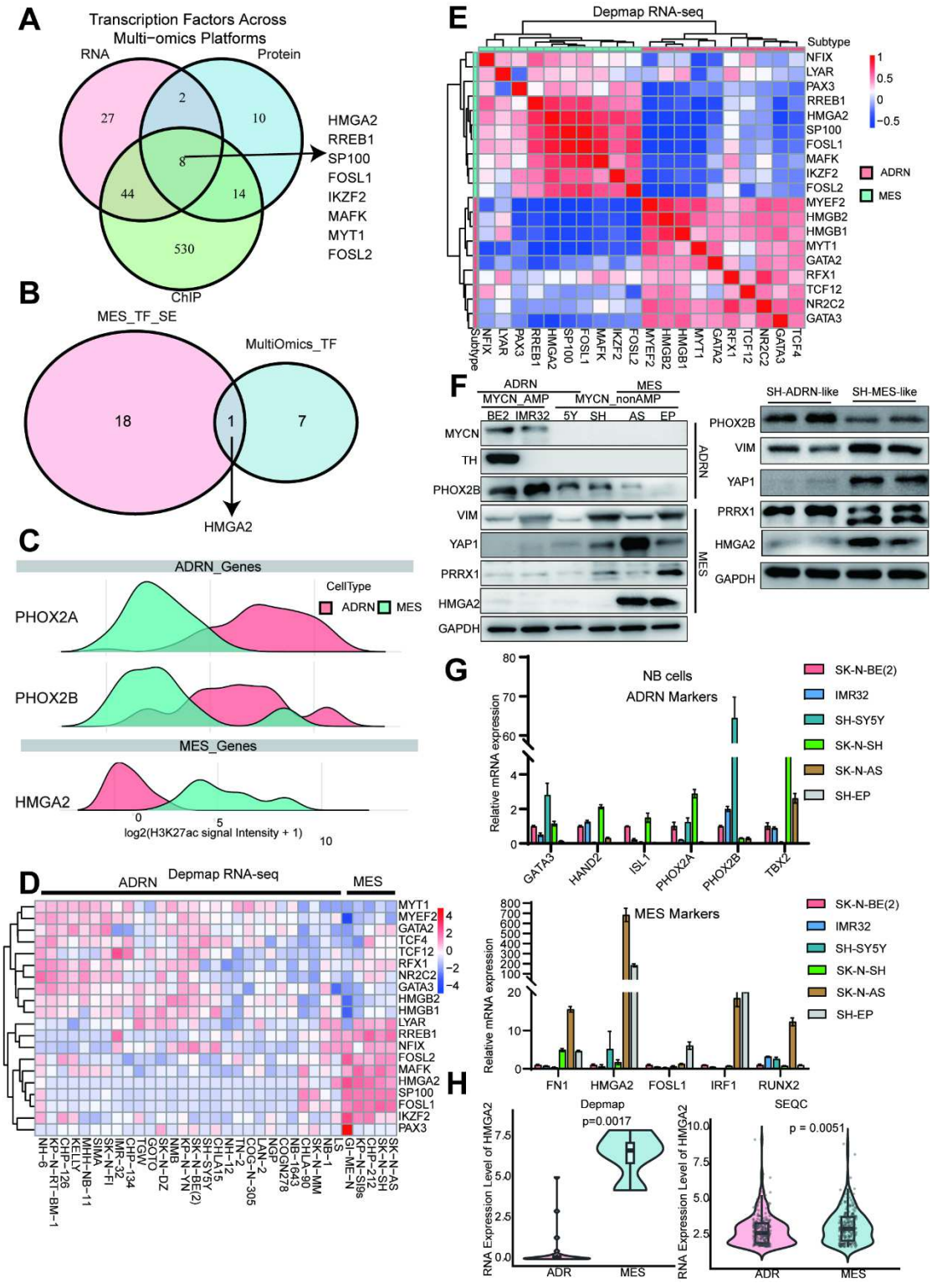


Fig. 1. Multi-omics identification of HMGA2 as a MES-associated transcriptional regulator in neuroblastoma.

(A) Venn diagram showing the overlap of differentially expressed transcription factors (TFs) identified from transcriptomic, proteomic, and H3K27ac ChIP seq datasets. HMGA2, FOSL1, and FOSL2 were consistently upregulated in MES cells across all three layers.

(B) Venn diagram illustrating the overlap between multi omics derived MES TFs and super enhancer (SE) associated TFs identified in three MES neuroblastoma cell lines.

(C) Density plots of H3K27ac ChIP seq signal intensity (log_2[signal+1]) at the HMGA2, PHOX2A, and PHOX2B genomic loci across six neuroblastoma cell lines (three MES and three ADRN).

(D) Heatmap of the top 10 upregulated and top 10 downregulated TFs between MES and ADRN states across 33 neuroblastoma cell lines (DEPMAP dataset). Rows are clustered by k means clustering.

(E) Correlation heatmap of transcriptomic expression among multi omics derived TFs, showing co expression patterns within each cellular state.

(F) Western blot analysis of HMGA2, VIM, and YAP1 protein expression across the indicated neuroblastoma cell lines.

(G) RT qPCR analysis of HMGA2 mRNA expression across a panel of neuroblastoma cell lines, classified as MES type (SH EP, SK N AS) or ADRN type (SH SY5Y, SK N BE2, IMR 32, NGP). Data are presented as mean ± SEM from three independent experiments.

(H) Violin plots showing HMGA2 expression distribution in the DEPMAP database (n = 33 cell lines) and the SEQC clinical dataset (n = 498).

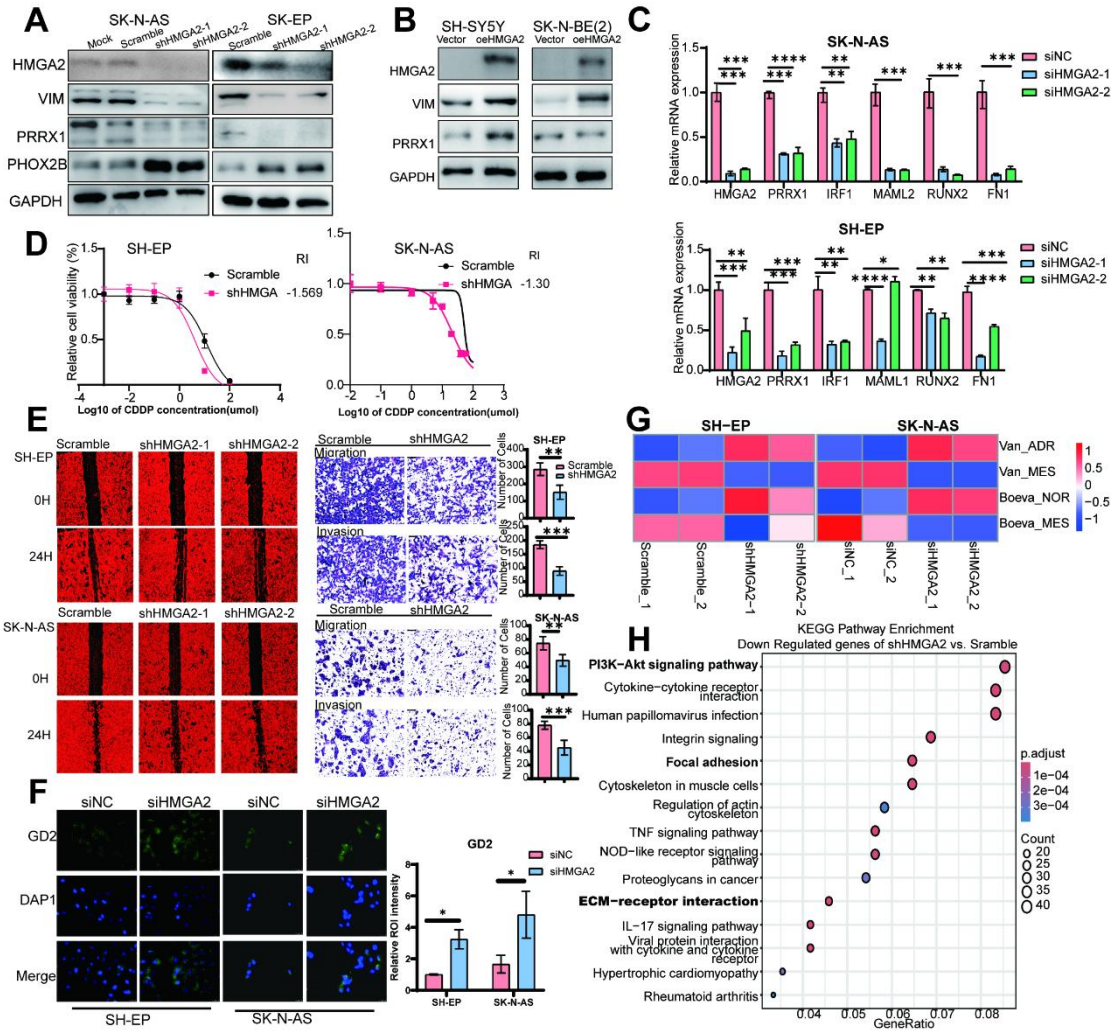


Fig. 2. HMGA2 sustains the MES phenotype and governs cellular state plasticity in neuroblastoma.

(A) Western blot analysis of MES markers (PRRX1, VIM) and the ADRN marker PHOX2B following HMGA2 knockdown (shRNA) in MES-type neuroblastoma cell lines (SK-N-AS and SH-EP). GAPDH served as loading controls.

(B) Western blot analysis of MES marker expression following ectopic HMGA2 overexpression in ADRN-type cell lines (SH-SY5Y and BE2), demonstrating partial MES-like reprogramming.

(C) RT-qPCR validation of MES-related transcription factors and marker genes after HMGA2 knockdown. Data are presented as mean ± SD from three independent experiments; *$p < 0.05$, **$p < 0.01$.

(D) Dose-response curves for cisplatin treatment following HMGA2 knockdown in SK-N-AS and SH-EP cells. IC50 values and the Resistance Index (RI = $\log_2$[IC50_KD / IC50_ctrl]) are indicated. Data represent mean ± SD from three independent experiments.

(E) Representative images of wound healing (left) and Transwell invasion (right) assays in HMGA2-knockdown MES cell lines. Scale bar, 200 μm. Data are presented as mean ± SD; ***$p < 0.001$.

(F) Immunofluorescence staining for the GD2 surface antigen in HMGA2-knockdown and control MES cell lines (SK-N-AS and SH-EP). Scale bar, 50 μm.

(G) Single-sample Gene Set Variation Analysis (ssGSEA) scores for ADRN and MES transcriptional signatures in HMGA2-knockdown versus control MES cells.

(H) KEGG pathway enrichment analysis of differentially expressed genes upon HMGA2 knockdown in MES cells.

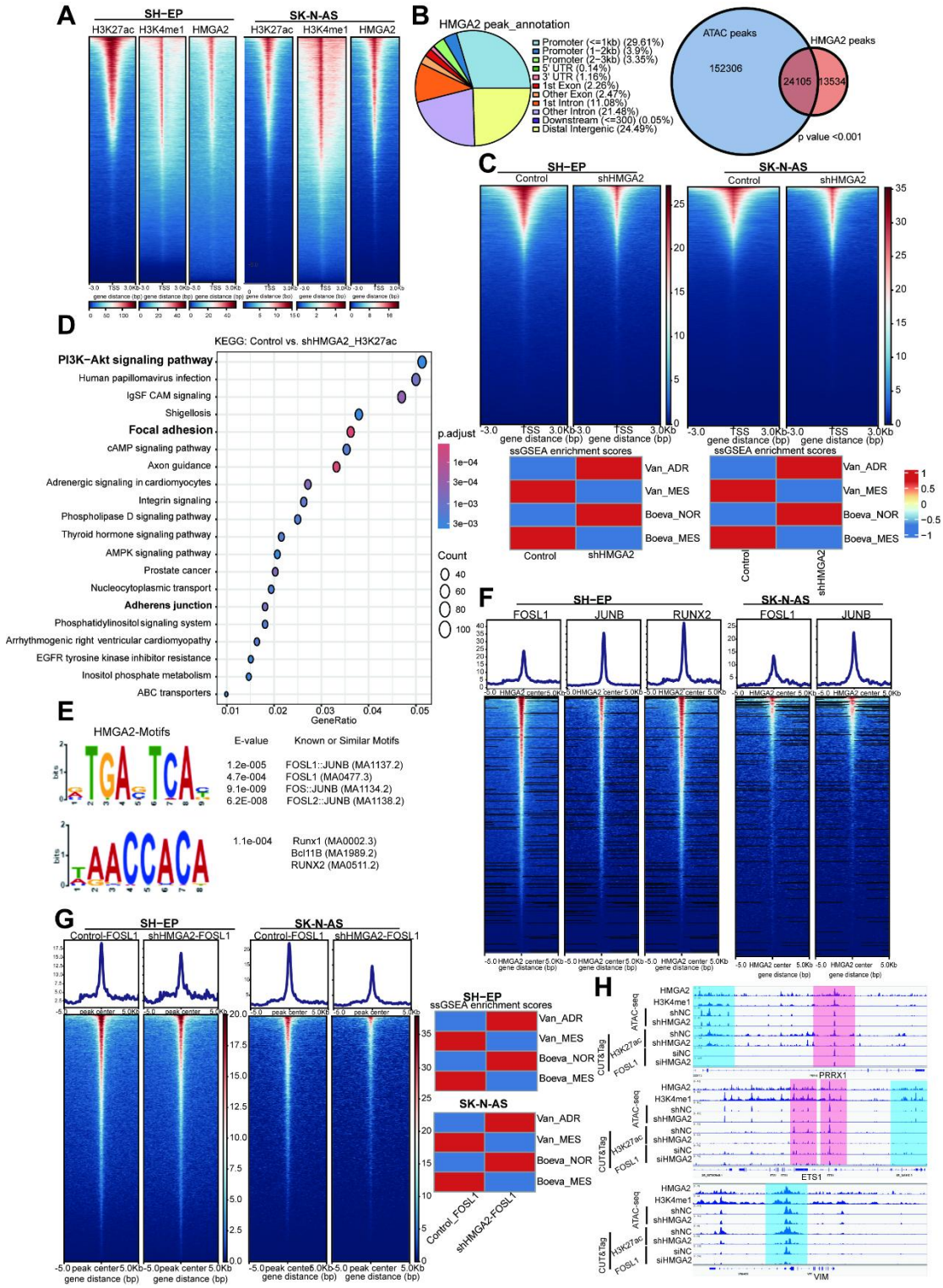


Fig. 3. HMGA2 maintains MES-specific chromatin accessibility and facilitates FOSL1 recruitment.

(A) Genome-wide HMGA2 CUT&Tag signal distribution in MES-state neuroblastoma cells, showing preferential localization of HMGA2 signals at accessible chromatin regions.

(B) Genomic annotation of HMGA2 binding sites and overlap analysis between HMGA2

CUT&Tag peaks and ATAC-seq peaks in SH-EP cells. p values are indicated.

(C) Heatmaps of H3K27ac CUT&Tag signals at promoter and enhancer regions in HMGA2-knockdown (shHMGA2) and control (shCtrl) MES cells. MES and ADRN ssGSEA scores derived from genes associated with decreased H3K27ac peaks are shown below.

(D) KEGG pathway enrichment analysis of genes associated with regions showing reduced H3K27ac signals after HMGA2 knockdown. Adjusted p values are indicated.

(E) De novo motif analysis of HMGA2 CUT&Tag peaks. Motif logos and E values are shown for AP-1 family members, including FOSL1, FOSL2, and JUNB, and for RUNX2.

(F) Heatmaps of FOSL1, JUNB, and RUNX2 CUT&Tag signal intensity centered on HMGA2 binding sites (±5 kb).

(G) Heatmaps of FOSL1 CUT&Tag signal intensity centered on HMGA2-bound regions in shHMGA2 and shCtrl MES cells.

(H) Representative IGV tracks at MES-associated loci in shHMGA2 and shCtrl MES cells. Baseline HMGA2 and H3K4me1 CUT&Tag tracks are shown as reference tracks, and ATAC-seq, H3K27ac CUT&Tag, and FOSL1 CUT&Tag tracks show HMGA2-dependent regulatory signal changes at representative loci.

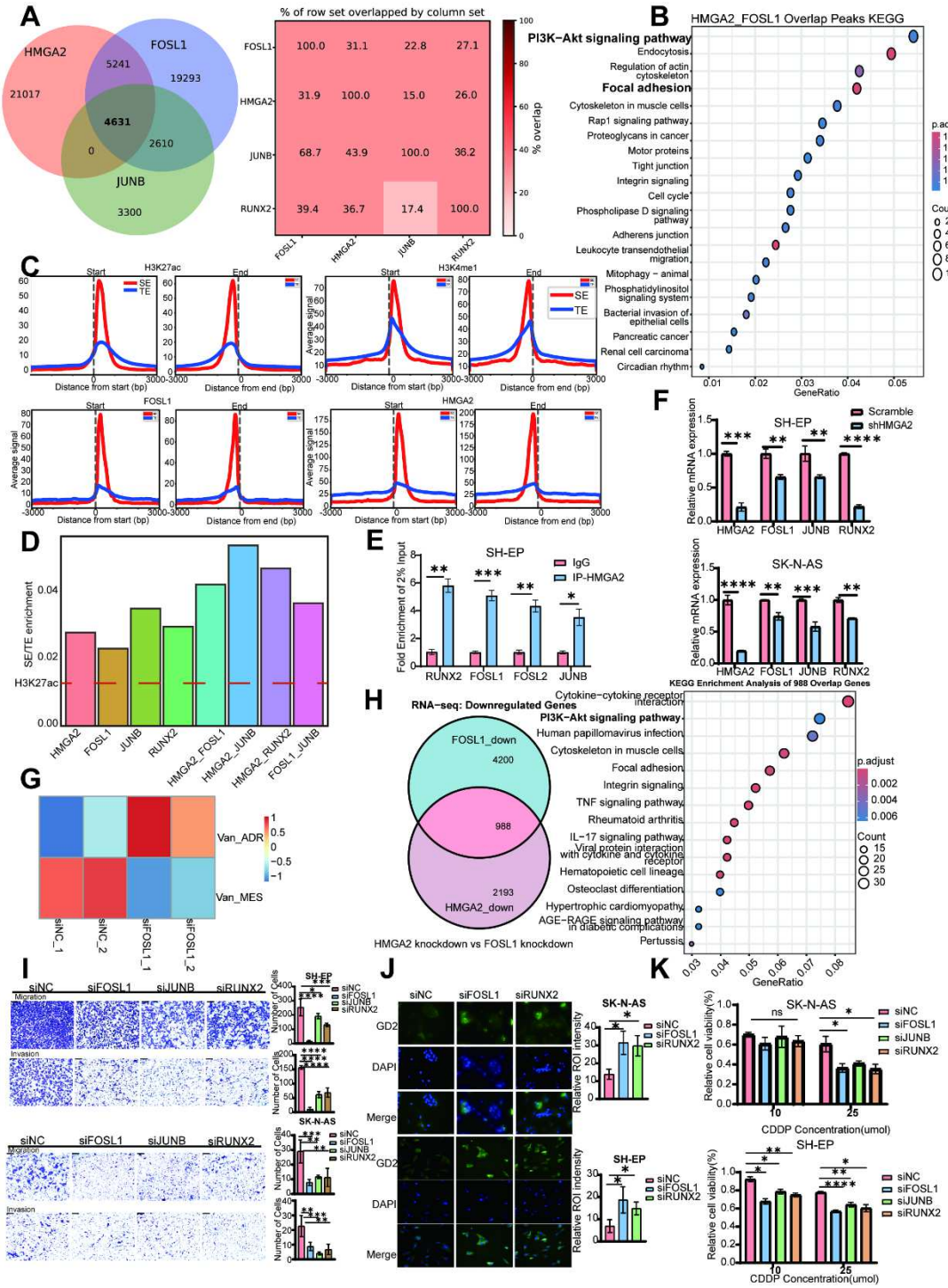


Fig. 4. The HMGA2-FOSL1 regulatory module reinforces MES malignancy through Super-Enhancer-Linked transcriptional amplification

(A) Overlap analysis of HMGA2, FOSL1, and JUNB CUT&Tag peaks in MES neuroblastoma cells, shown by Venn diagram and relationship heatmap.

(B) KEGG pathway enrichment analysis of genes co-bound by HMGA2 and FOSL1. Significantly enriched pathways included PI3K-AKT signaling, focal adhesion, and other MES-associated pathways.

(C) Boundary profiles of H3K27ac, H3K4me1, HMGA2, and FOSL1 signals around super-enhancer (SE) centers (±3 kb) in SH-EP cells.

(D) Bar plot showing SE/typical enhancer (SE/TE) enrichment ratios for individual factors (HMGA2, FOSL1, JUNB, and RUNX2) and co-bound peak sets (HMGA2-FOSL1 and HMGA2-JUNB), compared with the H3K27ac baseline.

(E) ChIP-qPCR analysis showing HMGA2 occupancy at regulatory regions of FOSL1, JUNB, and RUNX2 in MES cells. IgG served as a negative control. Data are presented as mean ± SD from three independent experiments; **$p < 0.01$, ***$p < 0.001$, ****$p < 0.0001$.

(F) RT-qPCR analysis of FOSL1, JUNB, and RUNX2 expression after HMGA2 knockdown in MES cells. Data are presented as mean ± SD from three independent experiments; *$p < 0.05$, **$p < 0.01$, ***$p < 0.001$.

(G) ssGSEA enrichment scores for MES and ADRN transcriptional signatures following FOSL1 knockdown in MES cell lines.

(H) Shared differentially expressed genes and pathway analysis between HMGA2-knockdown and FOSL1-knockdown cells, highlighting convergence on PI3K-AKT signaling, focal adhesion, and other MES-associated pathways.

(I) Transwell migration and invasion assays following knockdown of FOSL1, JUNB, or RUNX2 in MES neuroblastoma cells. Representative images and quantification are shown. Scale bar, 100 μm. Data are presented as mean ± SD; *$p < 0.05$, **$p < 0.01$, ***$p < 0.001$, ****$p < 0.0001$.

(J) Immunofluorescence staining for GD2 surface antigen following knockdown of FOSL1, JUNB, or RUNX2 in MES cells. GD2 expression was increased after depletion of these factors. Scale bar, 25 μm.

(K) Cisplatin dose-response curves in FOSL1-, JUNB-, and RUNX2-knockdown MES cells compared with vector control cells. IC50 values are indicated. Data are presented as mean ± SD from three independent experiments.

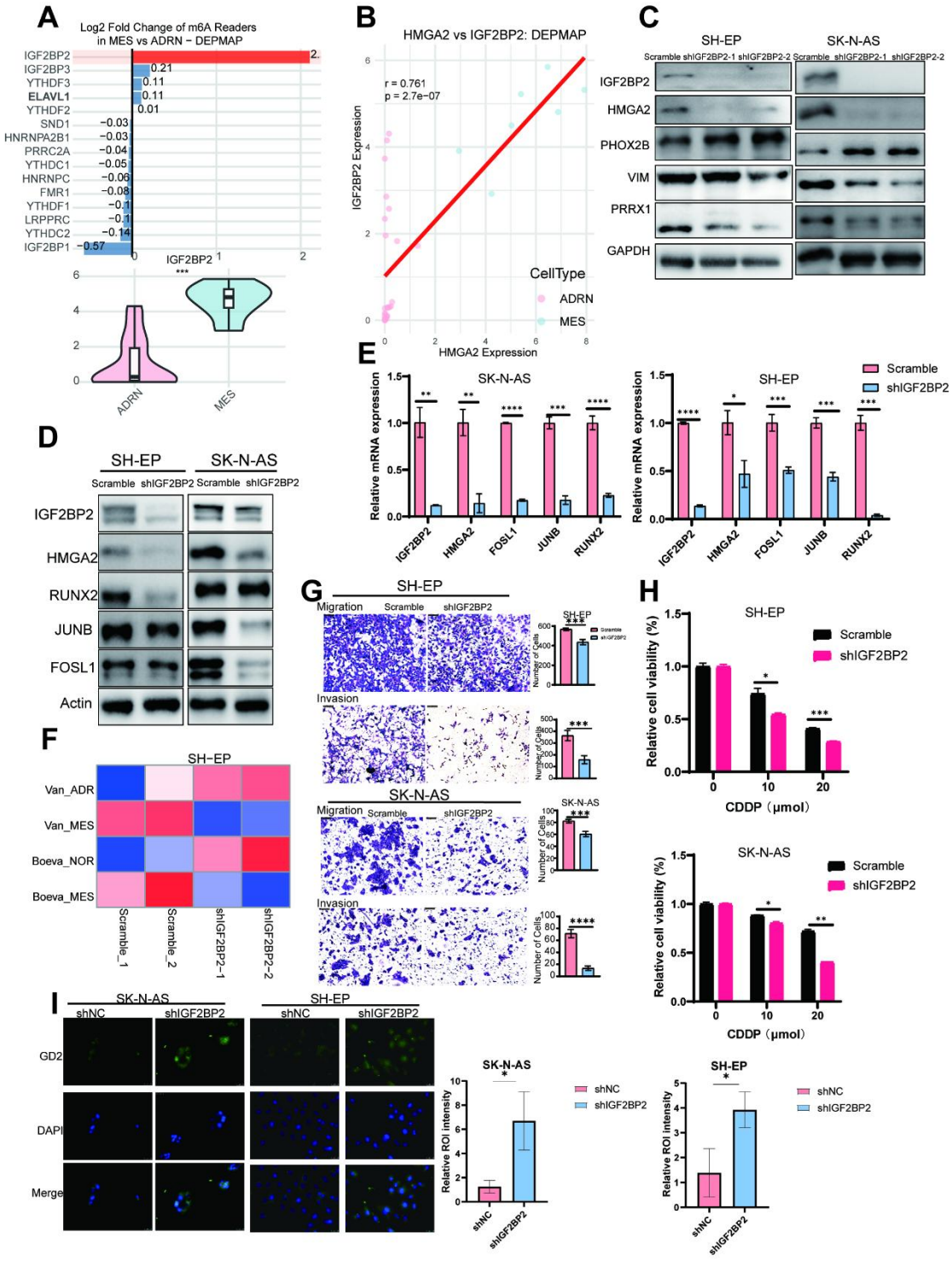


Fig. 5. IGF2BP2 sustains HMGA2 expression.

(A) Bar plot showing the differential expression of all RNA binding proteins (RBPs), with IGF2BP2 highlighted, between MES and ADRN neuroblastoma cells based on DepMap transcriptomic data.

(B) Scatter plot with Pearson's correlation coefficient showing the correlation between HMGA2 and IGF2BP2 expression levels in neuroblastoma cell lines.

(C–D) Western blot analysis of MES markers (HMGA2, VIM) and HMGA2 downstream transcription factors (FOSL1, JUNB, RUNX2) following IGF2BP2 knockdown.

(E) qPCR analysis of HMGA2 and its downstream transcription factors (FOSL1, JUNB, RUNX2) after IGF2BP2 knockdown.

(F) ssGSEA scores of MES and ADRN signatures derived from transcriptomic data following IGF2BP2 knockdown.

(G) Transwell assay images with quantification assessing cell invasion and migration capacities after IGF2BP2 knockdown. Scale bar = 100 μm.

(H) Cell viability assay (mean ± SEM) measuring the cytotoxic effects of cisplatin (CDDP) treatment after IGF2BP2 knockdown.

(I) Immunofluorescence images of GD2 staining (green) with DAPI nuclear counterstain (blue). Scale bar, 25 μm.

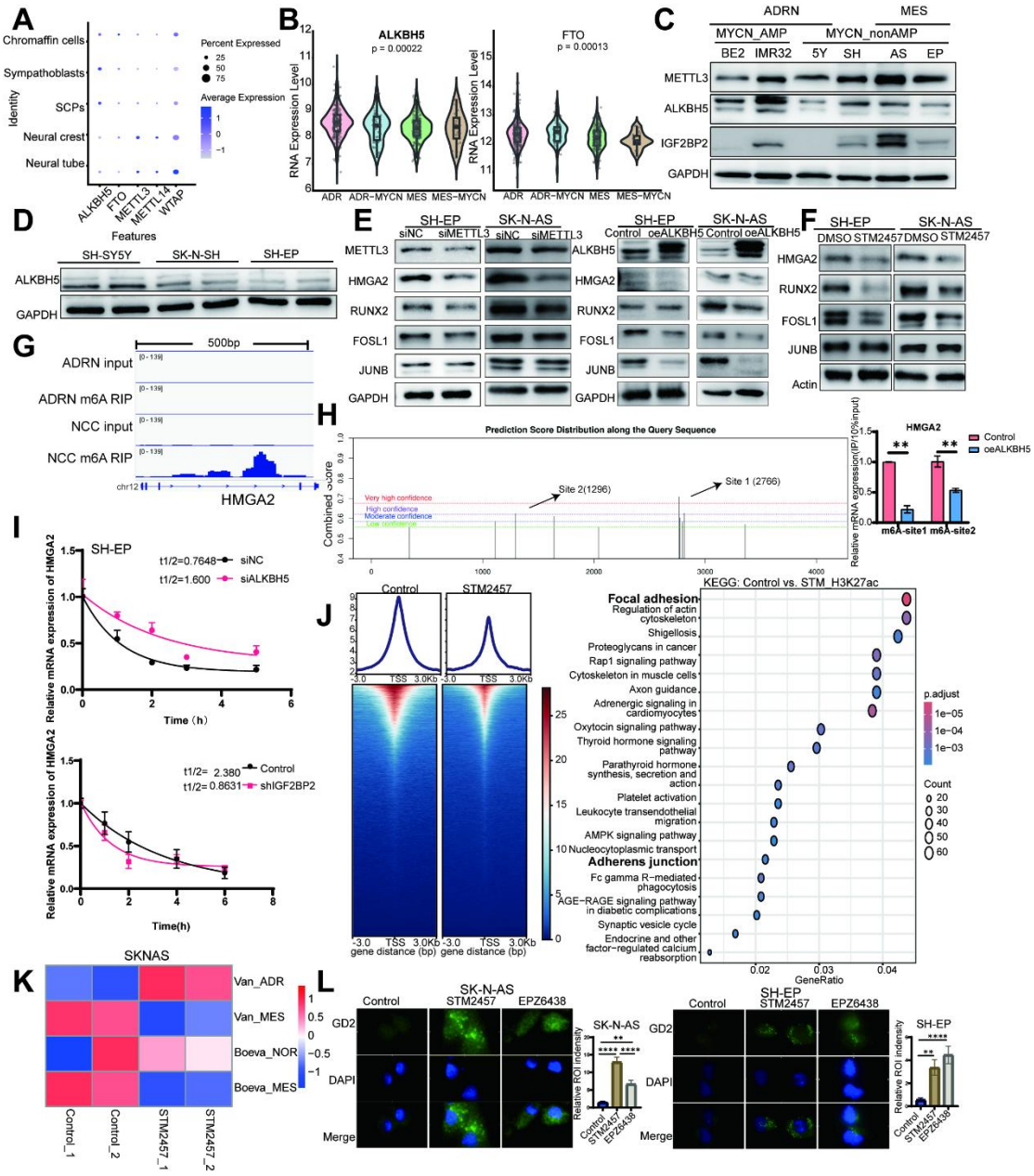


Fig. 6. RNA m⁶A modification modulates the IGF2BP2/HMGA2 axis in MES state maintenance.

(A) Dot plot from single cell transcriptomic data showing the expression of m⁶A associated genes (ALKBH5, FTO, METTL3) across ADRN and MES cellular states.

(B) Violin plots comparing ALKBH5 and FTO expression levels between ADRN and MES samples (SEQC dataset).

(C) Western blot analysis of ALKBH5, METTL3, and IGF2BP2 protein expression in six neuroblastoma cell lines.

(D) Western blot analysis of ALKBH5 protein expression in SH SY5Y, SK N SH, and SH EP

isogenic cell lines.

(E) Western blot analysis of HMGA2 and AP 1 family members following METTL3 knockdown or ALKBH5 overexpression in MES cells.

(F) Western blot analysis of HMGA2 and AP 1 family members after treatment with the METTL3 inhibitor STM2457 in MES cells.

(G) IGV tracks showing m^{6}A RIP sequencing signals at the HMGA2 coding region in neural crest cells (NCCs) and ADRN cell (SK-N-BE(2)), with the upper panel indicating the genomic locus.

(H) Schematic diagram of predicted m^{6}A sites within the HMGA2 transcript, and meRIP qPCR data (mean ± SEM, n = 3) showing m^{6}A enrichment ratios upon ALKBH5 overexpression.

(I) mRNA stability curves (mean ± SEM, n = 3) of HMGA2 following ALKBH5 or IGF2BP2 knockdown, measured by actinomycin D chase assay.

(J) Heatmap of H3K27ac CUT&Tag signals comparing control and STM2457 treated MES cells, and dot plot of KEGG pathways enriched among H3K27ac peaks downregulated by STM2457.

(K) Heatmap of ssGSEA scores for MES and ADRN signatures derived from transcriptomic data after STM2457 treatment.

(L) Immunofluorescence images of GD2 staining (green) with DAPI nuclear counterstain (blue) in MES cells after STM2457 and EPZ6438 treatment. Scale bar = 25 μm.

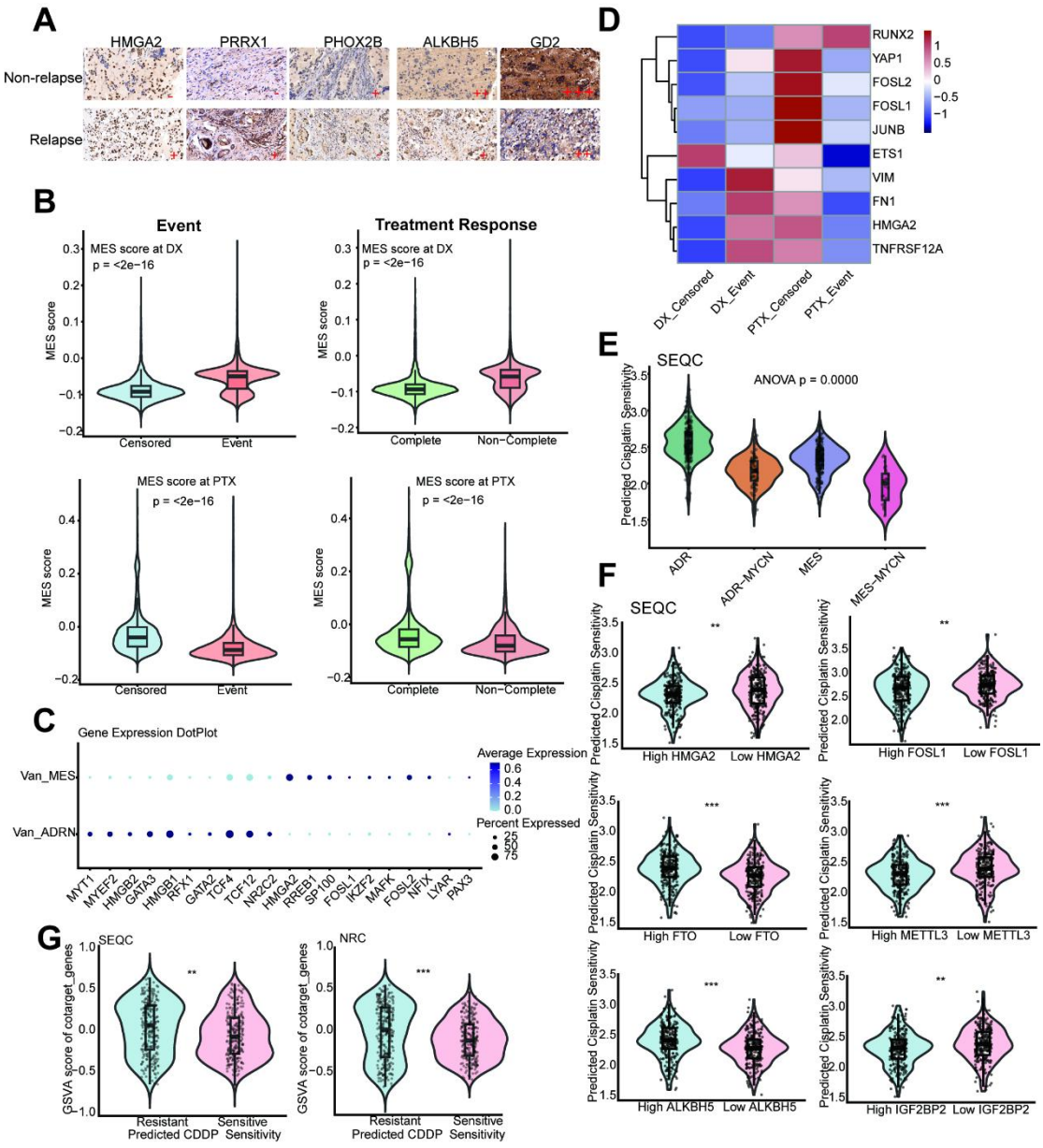


Fig. 7. Clinical implications of targeting the MES phenotype.

(A) Immunohistochemistry (IHC) analysis of HMGA2, GD2, PHOX2B, PRRX1 and ALKBH5 expression in paired primary and recurrent neuroblastoma tumor tissues.

(B) Violin plot showing the distribution of MES scores in pre chemotherapy (DX) and post chemotherapy (PTX) samples, stratified by clinical outcome (censored vs. event) and treatment response (complete vs. non complete).

(C) Dot plot depicting the expression of key transcription factors (HMGA2, FOSL1) across MES and ADRN cellular states in single cell transcriptomic data.

(D) Heatmap comparing the average expression levels of MES markers across four clinical groups (DX censored, DX event, PTX censored, and PTX event).

(E) Violin plots comparing predicted cisplatin sensitivity scores (derived from OncoPredict, SEQC cohort) between ADRN and MES dominant samples, further stratified by MYCN amplification status.

(F) Violin plots showing predicted cisplatin sensitivity scores stratified by high vs. low expression of HMGA2, FOSL1, IGF2BP2, ALKBH5, FTO, and METTL3 (SEQC cohort).

(G) Violin plots comparing GSVA scores for the HMGA2/FOSL1 co target gene set between cisplatin resistant and cisplatin sensitive patient samples.

Supplemental Figures

Supplemental Fig. 1.

(A) Principal component analysis (PCA) of transcriptomic, proteomic, and H3K27ac ChIP-seq data from neuroblastoma cell lines, demonstrating clear separation between ADRN and MES states across all molecular layers.

(B) H3K27ac ChIP-seq signal at super-enhancer regions, showing state-specific enrichment patterns in ADRN and MES cell lines.

(C) Volcano plot of transcriptomic data comparing MES versus ADRN neuroblastoma cell lines. HMGA2 is highlighted as one of the most significantly upregulated genes in MES cells (adjusted $p < 0.05$).

(D) Heatmap of the top differentially expressed TFs at the protein level, showing consistent MES/ADRN state separation.

(E) Protein-level correlation matrix of multi-omics-derived TFs, mirroring the transcriptomic co-expression patterns shown in Fig. 1E.

(F) Cisplatin (CDDP) IC50 values in MES versus ADRN cell lines.

(G) Flow cytometry histograms of GD2 expression in MES and ADRN cell lines (representative images; isotype control as reference).

Supplemental Fig. 2.

(A) Immunofluorescence staining of GD2 in ADRN-type (BE2, IMR32, SH-SY5Y) and MES-type (SK-N-AS, SH-EP) neuroblastoma cell lines. Scale bar, 50 μm.

(B) RT-qPCR analysis of HMGA2 and PHOX2B expression in MES-like and ADRN-like clones derived from the SK-N-SH cell line. Data are presented as mean ± SD.

(C) Dose-response curves for cisplatin treatment in MES-like and ADRN-like SK-N-SH clones. IC50 values were 18.75 μM and 6.95 μM, respectively. Data are presented as mean ± SD from three independent experiments.

(D) Wound healing assay comparing the migratory capacity of MES-like and ADRN-like clones. Representative images at 0 h and 24 h are shown. MES-like clones demonstrated significantly enhanced migration (***$p < 0.0001$).

(E) Flow cytometry analysis of GD2 surface expression in MES-like and ADRN-like SK-N-SH clones.

(F) Flow cytometry measuring EdU-positive cell proportion after HMGA2 knockdown.

(G) Flow cytometry analysis of GD2 surface expression in HMGA2-knockdown and control SK-N-AS and SH-EP cells.

(H) Dose-response curves for cisplatin treatment in HMGA2-overexpressing ADRN cell lines (SH-SY5Y and BE2), demonstrating increased cisplatin resistance relative to vector controls. IC50 values are indicated.

(I) ssGSEA enrichment scores for proliferative (cyc CHC, cyc SN) and non-proliferative (noncyc CHC, noncyc SN, SCPs) subgroup gene sets, as well as early developmental lineage states (neural tube [NTs] and EMT-associated neural crest cells [EMT-NCCs]), in HMGA2-overexpressing SK-N-BE(2) cells versus vector controls.

(J) Bidirectional bar plot showing limma t values calculated from KEGG pathway-level GSVA scores between MES and ADRN states. Positive and negative t values indicate pathways with higher activity scores in the corresponding comparison groups, and vertical dashed lines indicate the significance threshold.

(K) Bidirectional bar plot showing limma t values calculated from KEGG pathway-level GSVA scores comparing shHMGA2 and scramble control cells. Positive and negative t values indicate pathways with higher activity scores in the corresponding comparison groups, and vertical dashed lines indicate the significance threshold.

Supplemental Fig. 3.

(A) Unsupervised clustering of H3K27ac signals at HMGA2-bound regions.

(B) Pathway analysis of genes associated with H3K27ac signal clusters at HMGA2-bound regions. Cluster 1 genes were enriched in cell-matrix adhesion and embryonic development pathways, whereas cluster 2 genes were associated with basal cellular functions.

(C) ATAC-seq heatmaps and aggregate profiles in HMGA2-knockdown and control MES cells, centered on HMGA2 peaks.

(D) ATAC-seq-based MES and ADRN signature scores after HMGA2 knockdown, supporting a global loss of MES-specific chromatin accessibility.

(E) Additional representative IGV tracks showing HMGA2-dependent chromatin accessibility

and active chromatin changes at MES-associated loci.

(F) Heatmaps of FOSL1, JUNB, and RUNX2 CUT&Tag signals centered on transcription start sites (TSS; ±3 kb).

(G) Heatmaps of FOSL1 CUT&Tag signals at TSS regions in HMGA2-knockdown and control MES cells, showing reduced FOSL1 occupancy after HMGA2 depletion.

(H) Co-immunoprecipitation analysis assessing HMGA2 association with FOSL1 and JUNB in MES cells. IgG served as a negative control where applicable.

(I) Co-immunoprecipitation analysis confirming FOSL1-JUNB interaction in MES cells and comparison with the non-robust HMGA2-FOSL1 association under stringent conditions.

Supplemental Fig. 4.

(A) Heatmaps of JUNB CUT&Tag signals at HMGA2-bound regions and at TSS regions (±3 kb) upon HMGA2 knockdown, along with ssGSEA of MES/ADRN signatures for JUNB differential peaks, showing only a partial reduction in MES scores.

(B) KEGG dotplot of genes associated with differential JUNB CUT&Tag peaks upon HMGA2 knockdown, indicating enrichment in MES-associated pathways.

(C) Correlation scatter plots from DEPMAP showing significant negative correlations between HMGA2 expression and KDM1A and HDAC2 expression across neuroblastoma cell lines.

(D) Heatmaps of KDM1A CUT&Tag signal at TSS and HMGA2-bound regions in HMGA2-knockdown versus control MES cells, showing increased KDM1A occupancy upon HMGA2 depletion.

(E) Heatmap of KDM1A CUT&Tag signals at HMGA2-bound regions upon HMGA2 knockdown.

(F) Co-IP showing reduced KDM1A-HDAC2 interaction after HMGA2 depletion.

Supplemental Fig. 5

(A) Additional SE-centered signal profiles or heatmaps for HMGA2, FOSL1, JUNB, and RUNX2 in MES cells.

(B) Integrative IGV and Hi-C loop visualization of the VIM-associated super-enhancer region. Tracks show HMGA2, FOSL1, JUNB, and RUNX2 occupancy together with nearby super-enhancer annotations and chromatin-loop interactions, illustrating transcription factor binding at SE-associated regulatory regions.

(C) SpaMo analysis identifying a significant 7-bp spacing between FOSL1 and JUNB motifs

(E value = 0.0313, p = 1.77 x 10^-5) at HMGA2-FOSL1 co-bound regions, consistent with AP-1 heterodimer formation.

(D) H3K27ac CUT&Tag heatmap and aggregate profile after FOSL1 knockdown, showing reduced active chromatin signals at MES-associated regulatory regions.

(E) Western blot analysis of HMGA2 and AP-1 family protein expression after knockdown of FOSL1, JUNB, or RUNX2 in MES cells.

(F) ssGSEA scores for MES and ADRN transcriptional signatures following JUNB or RUNX2 knockdown in MES cells.

(G) Heatmap showing normalized RNA-seq read counts of AP-1 family genes, including FOSL1, FOSL2, JUNB, FOS, and JUN, and HMGA2 after FOSL1 or JUNB knockdown.

(H) ssGSEA enrichment scores for MES and ADRN signatures following genetic activation of the PI3K-Akt pathway in SK-N-FI cells.

Supplemental Fig.6.

(A) qPCR data for MES and ADRN markers after IGF2BP2 knockdown.

(B) Top panel: Western blot analysis of IGF2BP2 protein levels following HMGA2 knockdown (shHMGA2) and overexpression (OE HMGA2), indicating that HMGA2 positively regulates IGF2BP2 expression. Bottom left: ChIP qPCR showing the enrichment of HMGA2 at the IGF2BP2 promoter region, presented as percentage of input. Bottom right: Heatmap depicting the expression changes of HMGA2, IGF2BP2, and FOSL1 upon HMGA2 knockdown based on RNA seq counts.

(C) Barplot of t values from KEGG pathway GSVA analysis of differentially expressed genes upon IGF2BP2 depletion (adjusted $p < 0.05$). Pathways upregulated after IGF2BP2 silencing were enriched in ADRN associated processes, including DNA replication and mismatch repair.

(D) Cytotoxicity assay showing that CWI1 2, a specific IGF2BP2 inhibitor, Combination of 5 μM CWI1 2 with cisplatin (CDDP) synergistically enhanced cell killing.

(E) Transwell migration (Upper) and invasion (Lower) assays demonstrating that low dose CWI1 2 treatment significantly suppressed the migratory and invasive capacities of MES cells.

(F) Flow cytometry analysis of GD2 mean fluorescence intensity (MFI), revealing a mild upregulation of GD2 surface expression upon CWI1 2 treatment.

(G) Western blot analysis confirming that treatment with 1 μM CWI1 2 for 48 h markedly downregulated HMGA2 and other MES markers at the protein level.

(H) Venn diagram showing overlap between MES/ADRN state specific genes and m6A-RIP/ALKBH5 differential genes.

(I) Western blot (left) and qPCR (right) data for MES and ADRN markers after ALKBH5 or METTL3 knockdown, and after ALKBH5 overexpression.

Supplemental Fig. 7.

(A) CCK 8 bar plot (mean ± SEM) showing relative cell viability upon cisplatin (CDDP) treatment in MES cells following METTL3 knockdown or ALKBH5 overexpression, and in SK N BE2 cells following ALKBH5 knockdown

(B) Immunofluorescence images of GD2 staining (green) with DAPI nuclear counterstain (blue) in ADRN cells after ALKBH5 knockdown. Scale bar = 25 μm.

(C) Flow cytometry histograms showing the proportion of GD2 positive cells in SK N BE2 cells after ALKBH5 knockdown (isotype control shown as reference).

(D) Transwell invasion assay images with quantification (mean ± SEM) following ALKBH5 or METTL3 knockdown. Scale bar = 100 μm.

(E) CCK 8 bar plot (mean ± SEM) showing relative cell viability upon CDDP treatment after STM2457 treatment.

(F) Transwell assay images with quantification (mean ± SD) following STM2457 treatment. Scale bar = 100 μm.

(G) Flow cytometry histograms showing the proportion of GD2 positive cells in MES cells after STM2457 and EPZ6438 treatment (isotype control shown as reference).

(H) Bar plot of t values from KEGG GSVA analysis of transcriptomic data after STM2457 treatment (adjusted $p < 0.05$).

(I) Heatmap of ssGSEA scores for the Yuan_Trans poor prognosis signature and the Bexell_MES signature following METTL3 knockdown or STM2457 treatment.

Supplemental Fig. 8.

(A) Violin plots showing the single cell expression levels of HMGA2, IGF2BP2, and FOSL1 across ADRN and MES cellular states.

(B) Heatmap comparing the average expression of ADRN markers across DX censored, DX event, PTX censored, and PTX event groups.

(C) Bar plots showing the proportions of HMGA2, FOSL1, VIM, and YAP1 positive cells in DX censored vs. DX event samples.

(D) Heatmap illustrating the correlation between MES/ADRN signatures, HMGA2/FOSL1 co target gene expression, and predicted sensitivity to frontline chemotherapeutic agents (cisplatin, doxorubicin, vincristine) based on OncoPredict analysis.

(E) Violin plots of predicted cisplatin sensitivity scores (NRC cohort) for ADRN vs. MES patient samples, stratified by MYCN amplification status.

(F) Violin plots of predicted cisplatin sensitivity scores (NRC cohort) stratified by high vs. low expression of FOSL1, IGF2BP2, ALKBH5, or FTO.

(G) Kaplan Meier survival curves for overall survival (OS) and event free survival (EFS) in MES vs. ADRN cohorts, stratified by MYCN amplification status (SEQC and NRC databases). Log rank p values are indicated.

Supplementary Files

This is a list of supplementary files associated with this preprint. Click to download.

- SF8.tif
- SF1.tif
- SF6.tif
- SF2.tif
- SF3.tif
- SF7.tif
- SF5.tif
- SF4.tif
- supplementarytables13.docx
- qPCRdata.xlsx
- WB.docx